DEVICE TECHNOLOGY

Printed subthreshold organic transistors operating at high gain and ultralow power

Chen Jiang[1,2], Hyung Woo Choi[1], Xiang Cheng[1,3], Hanbin Ma[1,4,5], David Hasko[1], Arokia Nathan[1,3,5]*

Overcoming the trade-offs among power consumption, fabrication cost, and signal amplification has been a long-standing issue for wearable electronics. We report a high-gain, fully inkjet-printed Schottky barrier organic thin-film transistor amplifier circuit. The transistor signal amplification efficiency is 38.2 siemens per ampere, which is near the theoretical thermionic limit, with an ultralow power consumption of <1 nanowatt. The use of a Schottky barrier for the source gave the transistor geometry-independent electrical characteristics and accommodated the large dimensional variation in inkjet-printed features. These transistors exhibited good reliability with negligible threshold-voltage shift. We demonstrated this capability with an ultralow-power high-gain amplifier for the detection of electrophysiological signals and showed a signal-to-noise ratio of >60 decibels and noise voltage of <0.3 microvolt per hertz$^{1/2}$ at 100 hertz.

Organic thin-film transistors (OTFTs) have driven the development in low-cost, large-area electronics, including emerging application areas (*1*–*9*), such as wearable technologies. These applications require devices that can bend and stretch without affecting their electrical behavior (*10*, *11*). Organic semiconductors have been widely investigated for this application, but circuits usually require a large operating voltage, leading to high power consumption and unsuitability for battery-powered operation (*12*–*14*). The most challenging part of wearable electronics is the sensor interface, which is an analog application requiring low-voltage, low-power circuits with high gain, very high input impedance, low noise (*15*), and simple, low-cost fabrication (*16*, *17*).

To meet these requirements, we used an inkjet-printed circuit technology (*18*) with a subthreshold Schottky barrier OTFT (SB-OTFT) that operates near the off state. This approach has three main advantages (*19*). First, these transistors exhibit a steep subthreshold slope, which allows the use of a low operating voltage and leads to a high transconductance efficiency. Second, the current-voltage relation (*I-V*) characteristics are independent of the channel length for a broad range of device geometries. These characteristics are ideal for printed electronics, because the variation in the typical inkjet-printed feature size of ~40 μm can be as much as 10 μm (fig. S12). Third, the intrinsic gain of the SB-OTFT is large (e.g., >1000) and independent of channel length and electrical bias, with a *V-I* signal amplification efficiency approaching the theoretical limit of q/k_BT, where q is the elementary charge, k_B is Boltzmann's constant, and T is temperature.

Defect density must be minimized within the printed structure to ensure a good Schottky barrier contact at the source-semiconductor interface (*19*). The Schottky contact energy barrier for hole injection into the organic semiconductor is established by the difference between the work function of the metal and the highest occupied molecular orbit (HOMO) in the organic semiconductor (*19*–*21*). We used 2,7-dioctyl[1]benzothieno[3,2-b][1]benzothiophene (C8-BTBT)

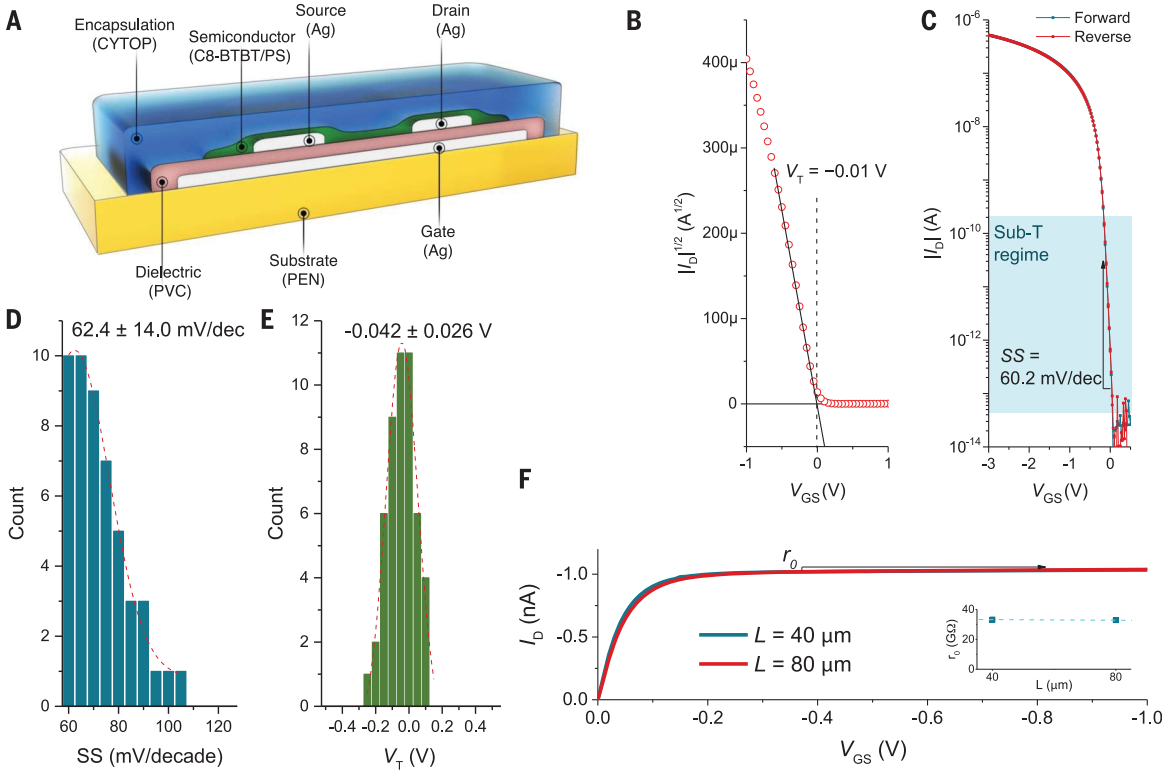

Fig. 1. Device structure and electrical characteristics. (**A**) Schematic cross section of the SB-OTFT. PS, polystyrene; PVC, polyvinyl cinnamate; PEN, polyethylene naphthalate. (**B** and **C**) Measured transfer characteristics (I_D versus V_{GS}) of a typical device (B) on a linear scale, indicating the threshold voltage (V_T), and (C) on a log scale, indicating the subthreshold slope (*SS*). dec, decade. (**D** and **E**) Statistical distributions of (D) *SS* and (E) V_T for 50 devices. The dashed lines indicate normal distributions. (**F**) Measured output characteristics (I_D versus V_{DS}) indicating the output resistance (r_o) of devices with different channel lengths (L) and showing a full overlap of the characteristics. The inset shows r_o versus L.

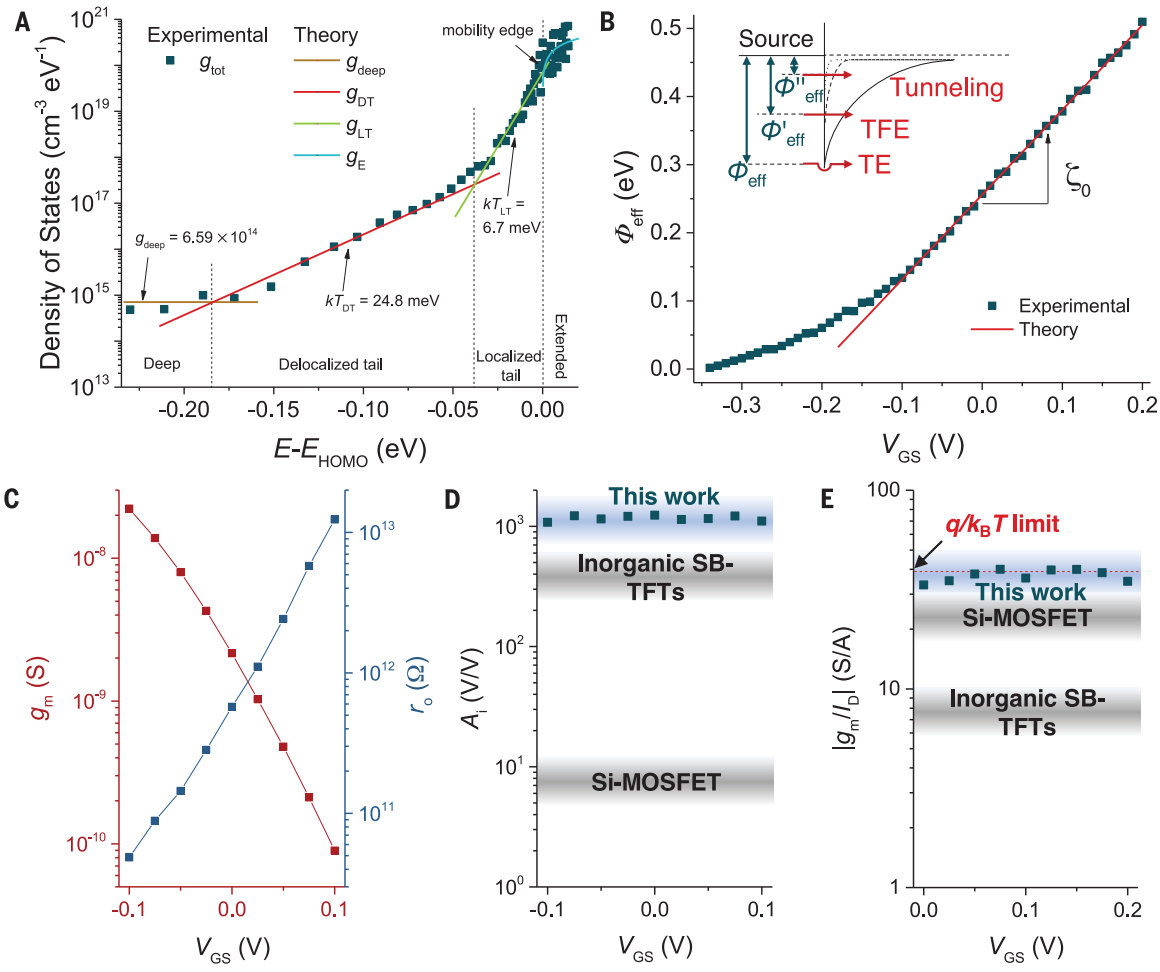

Fig. 2. Static parameters. (**A**) DOS for a typical device, indicating four different regimes: deep states, delocalized-tail (DT) states, localized-tail (LT) states, and extended (E) states. The slopes in the DT and LT regimes indicate the characteristic energies (k_BT_{DT} and k_BT_{LT}, respectively). g_{tot}, density of states. (**B**) Effective Schottky barrier heights (Φ_{eff}) as a function of V_{GS}, indicating the gate modulation factor (ζ_0) for the Φ_{eff} lowering. (Inset) Schematic energy band diagram showing variation in effective Φ_{eff} and different charge-carrier injection processes. TFE, thermionic field emission; TE, thermionic emission. (**C**) Experimental values for g_m and r_o as a function of V_{GS}. Ω, ohms. (**D**) Measured intrinsic gain (A_i) as a function of V_{GS}. Si-MOSFET, Si metal oxide semiconductor field-effect transistor. (**E**) Experimental values of transconductance efficiency (g_m/I_D) as a function of V_{GS}, reaching the theoretical thermionic limit of 38.7 S/A.

as the semiconductor (Fig. 1A), which exhibits fast growth (<1 min) of large crystals (>50 μm) and has a lower HOMO level than pentacene or other derivatives (*22*) to yield a good Schottky barrier (>0.2 eV) (*19*, *21*). Polyvinyl cinnamate was used as the dielectric layer to provide a smooth interface between the semiconductor and dielectric, thus minimizing carrier trapping and scattering (*23*). A fluoropolymer encapsulation layer (CYTOP) protected the device from environmental effects. Silver was used for the metal parts. All of these materials were formulated as inks with good jetting properties (fig. S1), and all of the fabrication steps for the individual SB-OTFTs and amplifier circuits reported here were carried out by using a single inkjet printer tool.

The SB-OTFT demonstrated a near-zero threshold voltage (V_T = −0.01 V) (Fig. 1B), along with an ultrasteep subthreshold slope of SS = 60.2 mV per decade (Fig. 1C) that approached the theoretical thermionic limit (*20*):

$$SS_{theoretical} = \ln(10)v_{th} = 59.6\frac{mV}{decade}(at\ T = 300\ K) \quad (1)$$

where $v_{th} = k_BT/q$ is thermal voltage. In addition, this steep SS is repeatable (fig. S3). The small V_T and steep SS resulted from the low trap density (*20*):

$$V_T = V_{T,theoretical} + \frac{Q_t}{C_i} \quad (2)$$

and

$$SS = SS_{theoretical}\left(1 + \frac{q^2D_t}{C_i}\right) \quad (3)$$

where Q_t is the trap carrier density in coulombs per square centimeter, D_t is the defect trap density per electron volt and square centimeter, and C_i is the gate insulator capacitance in farads per square centimeter. Q_t and D_t can be affected by defects in the semiconductor bulk (e.g., grain boundaries and stacking faults) and at the semiconductor-dielectric interface (e.g., interface roughness and atomic species or vacancies on dangling bonds). The relatively large semiconductor crystals in the thin-film transistor (TFT) channel (>50 μm, providing good coverage over the channel) (fig. S2E) substantially reduce grain boundaries and stacking faults, compared to those in the amorphous or micropolycrystalline phases. The printed polymer dielectric layer was free of dangling bonds and provided a smooth semiconductor-dielectric interface (with roughness of 2.1 Å) (fig. S2C). This was comparable to the roughness of the silicon–silicon dioxide interface in state-of-the-art complementary metal oxide semiconductor technologies. Thus, reducing the defect density to a very low level gives the best values for V_T and SS. Furthermore, the variation in these values between devices was much less than for other vacuum deposition–based TFT technologies (Fig. 1, D and E, and table S1). TFTs with a large C_i are effective in reducing V_T and SS (*24*) but lead to higher operating currents. Although this

[1]Electrical Engineering Division, Department of Engineering, University of Cambridge, 9 JJ Thomson Avenue, Cambridge CB3 0FA, UK. [2]Department of Clinical Neurosciences, University of Cambridge, Cambridge Biomedical Campus, Cambridge CB2 0QQ, UK. [3]Cambridge Touch Technologies, 154 Cambridge Science Park, Cambridge CB4 0GN, UK. [4]Suzhou Institute of Biomedical Engineering and Technology, Chinese Academy of Sciences, Suzhou 215163, China. [5]Acxel Tech, 184 Cambridge Science Park, Cambridge CB4 0GA, UK.
*Corresponding author. Email: an299@cam.ac.uk

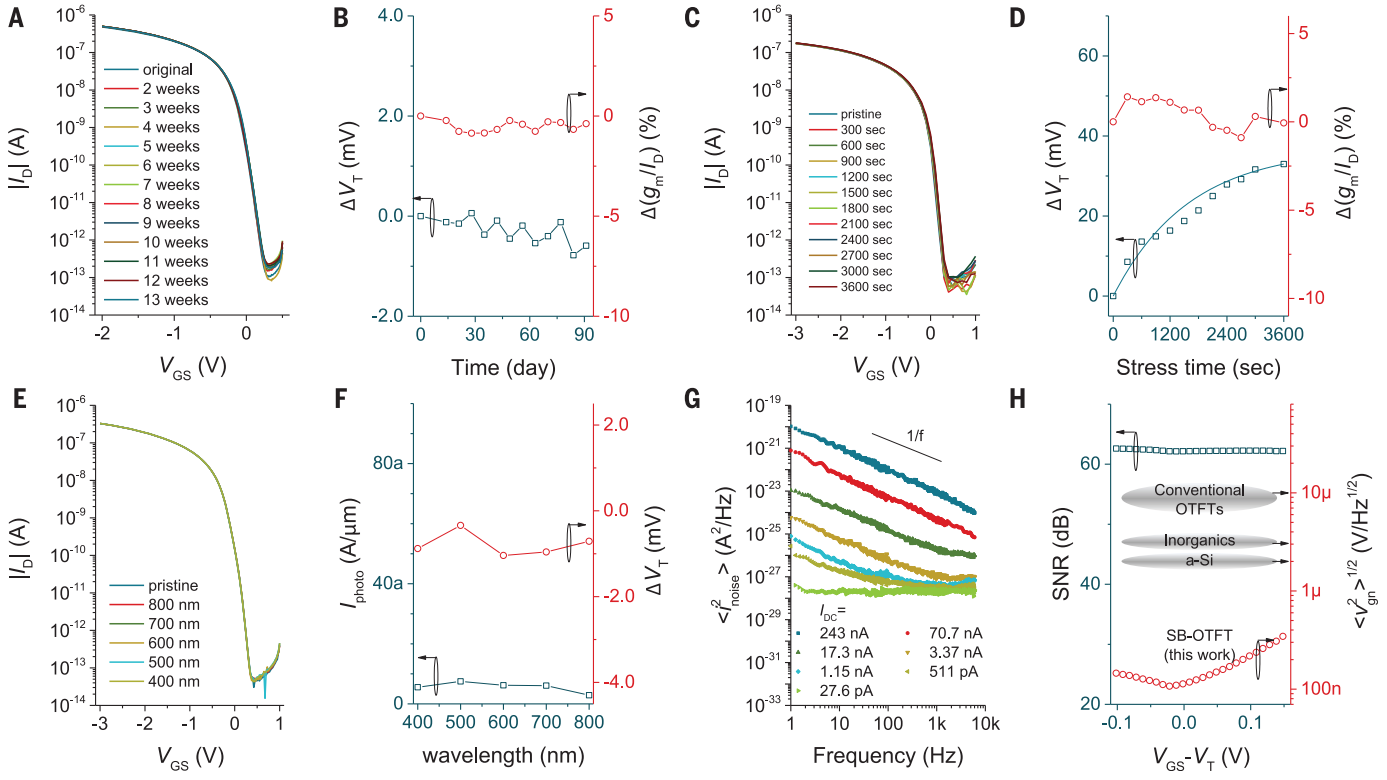

Fig. 3. Stability and reliability. (**A**) Measured transfer characteristics for a TFT in storage under ambient conditions for the times indicated and (**B**) change in absolute threshold voltage (ΔV_T) and change in relative transconductance efficiency [$\Delta(g_m/I_D)$] as a function of time. (**C**) Measured transfer characteristics under negative bias stress ($V_{GS} = V_{DS} = -3$ V) for the stress time indicated and (**D**) ΔV_T and $\Delta(g_m/I_D)$ as a function of stress time. (**E**) Measured transfer characteristics under light exposure and (**F**) photocurrent (I_{photo} in amperes per micrometer) and ΔV_T for different wavelengths (400 to 800 nm). (**G**) Measured SB-OTFT current noise under different direct current biases (I_{DC}). (**H**) SNRs in the near-threshold and subthreshold regimes and input-referred voltage noise density at 100 Hz. a-Si, amorphous silicon.

boosts the switching speed in logic circuits, it does not benefit the low-power, low-frequency operation of analog sensor interfaces.

We investigated the nature of the defect density and of the Schottky barrier through the density of states (DOS) (see Fig. 2A) and the effective Schottky barrier height (Φ_{eff}). These results suggest that the DOS comprises a small and constant background of deep states ($g_{deep} = 6.59 \times 10^{14}$ cm^{-3} eV^{-1}, where g_{deep} is deep-state density), a broad spectrum of delocalized states with a characteristic energy of 24.8 meV near v_{th}, and a steeply rising number of localized tail states with a characteristic energy of 6.7 meV. In addition, because the DOS was dominated by extended states (according to $\sqrt{E - E_{HOMO}}$, where E is energy), there was a clear mobility edge for energies above the HOMO level (i.e., $E > E_{HOMO}$), characteristic of a small overall DOS. Because the semiconductor surface potential (φ_S) cannot be neglected in low-voltage TFTs, this term was included in the DOS calculation (eqs. S5 to S23).

The source-side Schottky barrier height (Φ_{eff}) decreased with increasing $-V_{GS}$, so that the drain current (I_{DS}) was modulated by the gate bias. Φ_{eff} could be extracted from temperature-dependent I-V measurements (fig. S6). In the subthreshold regime, $\Phi_{eff} = \zeta_0 V_{GS} + \Phi_{eff,0}$, where ζ_0 is a coefficient that describes the modulation of Schottky barrier height by V_{GS} (*19*). Φ_{eff} showed a good initial Schottky barrier of ~0.51 eV and a high barrier-lowering factor of $\zeta_0 = 1.24$. This result suggests that charge-carrier injection was mainly by thermionic emission, with smaller contributions from thermionic field emission and tunneling (see the inset of Fig. 2B). Above a certain V_{GS} level (in the case shown at –0.34 V), barrier lowering saturated and the transistor behaved ohmically in the above-threshold regime. This change occurred when the source-side depletion width reached just a few nanometers and allowed charge carriers to tunnel through the Schottky barrier (fig. S5C) (*20*, *21*). The small defect density and the presence of a good Schottky barrier in the subthreshold regime were prerequisites for high transconductance (mutual conductance g_m) and output resistance (r_o).

The near-zero V_T was important for low-power operation, whereas the ultrasteep *SS* was important for high transconductance ($g_m = \partial I_{DS}/\partial V_{GS}$) and transconductance efficiency (g_m/I_{DS}) (eqs. S2 and S3). In addition, the SB-OTFT operation was channel-length independent with a large output resistance ($r_o = \partial V_{DS}/\partial I_{DS}$) (Fig. 1F), which was provided by the Schottky barrier at the source-semiconductor contact. Thus, the SB-OTFT could provide a high intrinsic gain (defined as $A_i = g_m r_o$) (*25*) resulting from the high transconductance and output resistance.

Both the transconductance and output resistance had an exponential dependence, with an inverse proportionality, on $-V_{GS}$ because of the response of SB-TFTs in the subthreshold regime (Fig. 2C), as was also the case previously with an inorganic SB-TFT (*19*). In comparison with other TFT technologies, the SB-OTFT transconductance and output resistance are about 10 times as high at similar currents: $g_m = 3.8 \times 10^{-8}$ S and $r_o = 3.2 \times 10^{10}$ ohms at $I_{DS} = 1$ nA (*1*–*6*, *24*, *26*–*28*). The intrinsic gain A_i was determined from the theoretical expression (*19*) $A_i = \frac{SS_{theoretical}}{SS} n \exp\left(\frac{v_{sat}}{nv_{th}}\right)$, where n is the ideality factor (here, $n = 1.6$). These devices showed a high and constant value for A_i of ~1100 in the subthreshold regime (Fig. 2D), which is much larger than that of the inorganic SB-TFT and Si metal oxide semiconductor field-effect transistor because of the ultrasteep *SS*. More notably, g_m/I_{DS} for the SB-OTFT was ~38.2 S/A, approaching the theoretical limit for TFT technologies of q/k_BT (i.e., 38.7 S/A at $T = 300$ K). The high g_m/I_{DS} (indicating a large g_m at low I_{DS}) was essential for an amplifier circuit to achieve high gain at low power. The SB-OTFT reported here

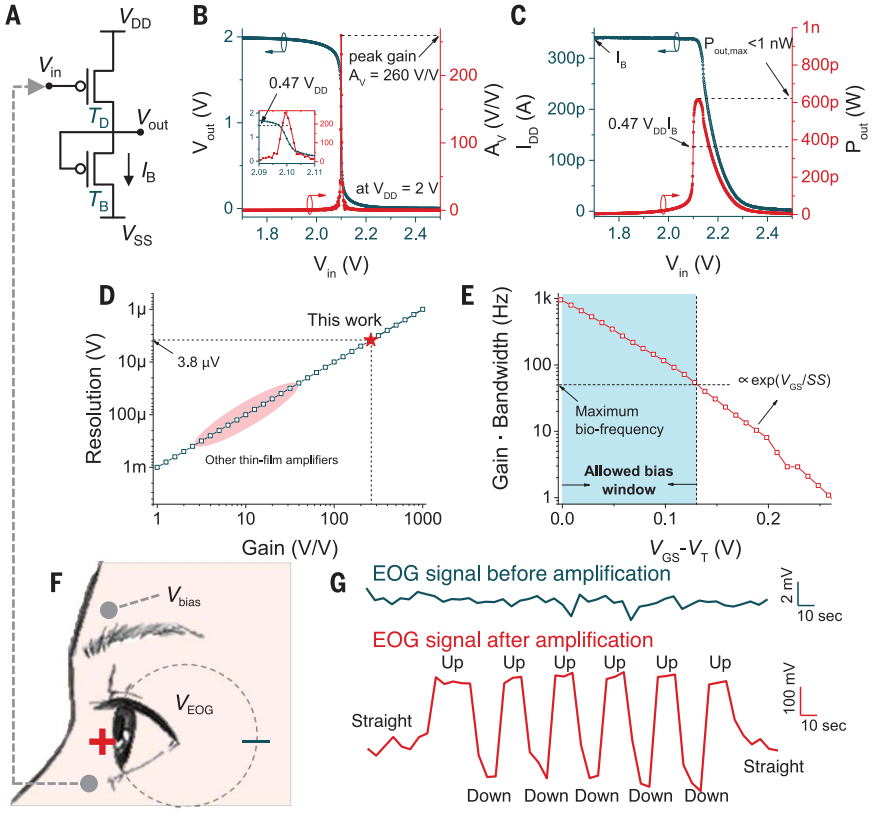

Fig. 4. Amplifier characteristics and demonstration of EOG detection. (**A**) Schematic circuit diagram of a common-source amplifier. V_{DD}, supply voltage; I_B, bias current. (**B**) Measured output voltage (V_{out}) and gain (A_V) as a function of input voltage (V_{in}). (**C**) Measured operating current (I_{DD}) and power (P_{out}) as functions of V_{in}. (**D**) Resolution of electrophysiological signal detection as a function of gain. (**E**) Gain-bandwidth product as a function of V_{GS} in the subthreshold regime. (**F**) Operating principle and circuit configuration for EOG amplification with the amplifier. (**G**) EOG signal obtained before and after amplification.

exhibited more efficient *V-I* signal amplification than the other reported devices (Fig. 2E).

The usability of inkjet-printed OTFTs is commonly limited by their short shelf life and operational instabilities (*29*, *30*). However, when the transfer (I_D-V_{GS}) characteristics of representative SB-OTFTs were tested over a period of 3 months under ambient conditions, no appreciable changes were observed (Fig. 3A). The threshold voltage shift was <1 mV, and the transconductance efficiency changed by <1%; thus, these SB-OTFTs were far superior under ambient environment operation and storage conditions than typical OTFTs, where these changes are generally >100 mV and >20%, respectively (*30*, *31*).

Similarly, the effect of electrical and illumination stress was very small (*29*–*31*). Electrical stress was applied under an on-state condition (i.e., V_{GS} = V_{DS} = −3 V), in which a conducting channel was formed and charge carriers were more likely to be trapped than in the nearly off-state condition. The transfer characteristics of the device before and after stress were almost identical (Fig. 3C). The threshold voltage shifted by <30 mV with a characteristic decay time of ~10^3 s, and the transconductance efficiency changed by <2% (Fig. 3D). Because of the wide bandgap of C8-BTBT (fig. S7), the device demonstrated good light stability (Fig. 3E) under visible-light illumination stress (10 mW/cm^2), with a photocurrent of <10 aA/μm and a threshold voltage shift within 1 mV (Fig. 3F).

Noise ultimately limits the minimum detectable signal in any circuit, especially at the low frequencies of many electrophysiological signals (<100 Hz). The low-frequency noise response of SB-OTFTs showed both 1/*f* (where *f* is frequency) and white noise (Fig. 3G). As expected, these noise components were proportional to the current as I^2 and I, respectively (fig. S8, C and D, and eqs. S29 and 30). Thus, by operating in the subthreshold regime, the noise was reduced, giving rise to a signal-to-noise ratio (SNR) of 63 dB over the cutoff frequency of the TFT (Fig. 3H), which is sufficient for most low-frequency analog applications. The flicker noise coefficient is fabrication process dependent, and the value in our devices was 1.8 × 10^{-22} V^2/F, which is one order of magnitude lower than that found in typical amorphous Si- and metal oxide–based TFTs and two orders of magnitude lower than that in conventional OTFTs (table S1) (*32*). The root-mean-square noise voltage referred to the gate $\sqrt{\langle v_{gn}^2 \rangle}$ for all noise sources is <0.3 μV/Hz$^{1/2}$ at 100 Hz (Fig. 3H), which is a few orders of magnitude lower than that of other TFT technologies for the same operating current.

We integrated amplifier circuits from pairs of SB-OTFTs in a common-source configuration, a drive transistor T_D and a bias transistor T_B (Fig. 4A). Because of the very high A_i of the SB-TFT, the amplifier demonstrated steep output voltage (V_{out}) characteristics and a voltage gain (A_V = $\partial V_{out}/\partial V_{in}$, where V_{in} is input voltage) of 260 V/V at the peak (Fig. 4B). Because transistor T_B operated in the subthreshold regime with a bias current I_B = 342 pA in the saturation regime, the power consumption was <1 nW (Fig. 4C). Compared to other TFT amplifiers, this high-gain amplifier enabled high resolution (<4 μV) of electrophysiological signal detection (Fig. 4D). In addition, the gain-bandwidth product was scalable by gate bias. Given a maximum electrophysiological signal frequency of 50 Hz (*33*), the SB-OTFT had a relatively large allowed bias window for analog circuit design (0.13 V) compared to the variation of V_T.

Such an amplifier can be used to monitor human electro-oculogram (EOG) signals, which are essentially the corneo-retinal potentials (V_{EOG}) that exist across the front (positive) and back (negative) of the human eye (Fig. 4F), typically in the range from 0.2 to ~1.0 mV (*34*). This technique is useful for eye movement tracking, particularly in improving existing technologies that are bulky and costly and require high power (*35*). With a biasing electrode over the eyebrow and another electrode below the lower eyelid connecting to the amplifier input (Fig. 4, A and F), the V_{in} relation for the amplifier becomes

$$V_{in} = V_{bias} + \gamma V_{EOG}. \quad (4)$$

Here, γ is a coefficient that describes the direction of eye movement. In the configuration used, γ < 0 corresponds to an upward movement of the eyeball, whereas γ > 0 indicates the corresponding downward movement. Therefore, the amplifier output gives an amplitude of up to ~0.3 V (Fig. 4G and movie S1). The amplifier is also able to track horizontal eye movement (fig. S11). The amplified EOG signal with amplitudes of >0.2 V and SNRs of >60 dB has the potential to detect subtle eye movements for a better depiction of the virtual environment (e.g., depth-of-field rendering). Tracking eye movement is important in virtual and augmented reality (*35*). The ultralow power consumption of SB-OTFT–based circuits means that they can potentially operate from energy acquired from microharvesters (on the order of microjoules per cycle) (*8*), although from a complete system standpoint this would require low-power versions of signal-conditioning and transmission circuit stages.

REFERENCES AND NOTES

1. R. A. Street, *Adv. Mater.* **21**, 2007–2022 (2009).
2. A. Nathan *et al*., *Proc. IEEE* **100**, 1486–1517 (2012).
3. K. Nomura *et al*., *Science* **300**, 1269–1272 (2003).
4. J. F. Wager, *Science* **300**, 1245–1246 (2003).
5. D. H. Kim *et al*., *Science* **333**, 838–843 (2011).
6. T. Someya, Z. Bao, G. G. Malliaras, *Nature* **540**, 379–385 (2016).
7. A. Campana, T. Cramer, D. T. Simon, M. Berggren, F. Biscarini, *Adv. Mater.* **26**, 3874–3878 (2014).
8. D. Khodagholy *et al*., *Nat. Commun.* **4**, 1575 (2013).
9. Y. Kim *et al*., *Science* **360**, 998–1003 (2018).
10. T. Sekitani, U. Zschieschang, H. Klauk, T. Someya, *Nat. Mater.* **9**, 1015–1022 (2010).
11. J. Xu *et al*., *Science* **355**, 59–64 (2017).
12. H. Nishide, K. Oyaizu, *Science* **319**, 737–738 (2008).
13. P. D. Mitcheson, E. M. Yeatman, G. K. Rao, A. S. Holmes, T. C. Green, *Proc. IEEE* **96**, 1457–1486 (2008).
14. W. Gao *et al*., *Nature* **529**, 509–514 (2016).
15. T. Sekitani *et al*., *Nat. Commun.* **7**, 11425 (2016).
16. H. Sirringhaus *et al*., *Science* **290**, 2123–2126 (2000).
17. L. Feng, C. Jiang, H. Ma, X. Guo, A. Nathan, *Org. Electron.* **38**, 186–192 (2016).
18. M. Singh, H. M. Haverinen, P. Dhagat, G. E. Jabbour, *Adv. Mater.* **22**, 673–685 (2010).
19. S. Lee, A. Nathan, *Science* **354**, 302–304 (2016).
20. S. M. Sze, *Physics of Semiconductor Devices* (Wiley, ed. 2, 1981).
21. Y. Xu, H. Sun, Y.-Y. Noh, *IEEE Trans. Electron Devices* **64**, 1932–1943 (2017).
22. M. Kano, T. Minari, K. Tsukagoshi, *Appl. Phys. Lett.* **94**, 143304 (2009).
23. C. Jiang, H. Ma, D. G. Hasko, X. Guo, A. Nathan, *Adv. Electron. Mater.* **3**, 1700029 (2017).
24. H. Klauk, U. Zschieschang, J. Pflaum, M. Halik, *Nature* **445**, 745–748 (2007).
25. B. Razavi, *Design of Analog CMOS Integrated Circuits* (McGraw-Hill, 2001).
26. M. J. Powell, *IEEE Trans. Electron Devices* **36**, 2753–2763 (1989).
27. S. D. Brotherton, *Semicond. Sci. Technol.* **10**, 721–738 (1995).
28. R. Martins *et al*., *Adv. Mater.* **23**, 4491–4496 (2011).
29. W. H. Lee, H. H. Choi, D. H. Kim, K. Cho, *Adv. Mater.* **26**, 1660–1680 (2014).
30. H. Sirringhaus, *Adv. Mater.* **21**, 3859–3873 (2009).
31. X. Jia, C. Fuentes-Hernandez, C.-Y. Wang, Y. Park, B. Kippelen, *Sci. Adv.* **4**, eaao1705 (2018).
32. T. Moy *et al*., *IEEE J. Solid-State Circuits* **52**, 309–321 (2017).
33. D. Mantini, M. G. Perrucci, C. Del Gratta, G. L. Romani, M. Corbetta, *Proc. Natl. Acad. Sci. U.S.A.* **104**, 13170–13175 (2007).
34. M. Brown *et al*., *Doc. Ophthalmol.* **113**, 205–212 (2006).
35. S. Hillaire, A. Lécuyer, R. Cozot, G. Casiez, "Using an eye-tracking system to improve camera motions and depth-of-field blur effects in virtual environments," in *2008 IEEE Virtual Reality Conference*, Reno, NV, 8 to 12 March 2008 (IEEE, 2008), pp. 47–50.

ACKNOWLEDGMENTS

Funding: We are grateful for the generous support from EPSRC under project EP/M013650/1 and the EU under projects DOMINO 645760, 1D-NEON 685758, and BET-EU 692373. C.J. acknowledges doctorate scholarship support from the China Scholarship Council (CSC) and the Cambridge Commonwealth, European and International Trust and fellowship support from the IEEE Electron Device Society. **Author contributions:** C.J., H.W.C., X.C., H.M., and A.N. conceived of and designed the overall experiments. C.J. and H.W.C. carried out experiments and collected related data. C.J. was the only human subject for the eye tracking study, and H.W.C. recorded the experiment. X.C. and C.J. contributed to circuit simulation and theoretical analysis. C.J., H.W.C., and A.N. initiated the study. C.J., H.W.C., X.C., H.M., D.H., and A.N. analyzed all the data and co-wrote the paper. All authors discussed the results and commented on the manuscript. **Competing interests:** The authors declare no competing interests. **Data and materials availability:** All data are available in the main text or the supplementary materials.

SUPPLEMENTARY MATERIALS

www.sciencemag.org/content/363/6428/719/suppl/DC1
Materials and Methods
Supplementary Text
Figs. S1 to S12
Tables S1 and S2
References (*36*–*61*)
Movie S1

14 October 2018; accepted 15 January 2019
10.1126/science.aav7057

Printed subthreshold organic transistors operating at high gain and ultralow power

Chen Jiang, Hyung Woo Choi, Xiang Cheng, Hanbin Ma, David Hasko and Arokia Nathan

Science **363** (6428), 719-723.
DOI: 10.1126/science.aav7057

Low-power organic transistors

For internet-of-things applications, transistors that deliver high signal amplification (high gain) at low power will help conserve power and extend battery life. Jiang *et al.* used inkjet printing to fabricate an organic transistor in which silver metal contacts form a low Schottky barrier (less than 0.2 electron volt) with an organic semiconductor. The transistor delivered gain near the theoretical limit at a power below 1 nanowatt and detected electrophysiological signals from the skin with a wearable device.

Science, this issue p. 719